

Chapter 1

Waveguide Evanescent Field Fluorescence and Scattering Microscopy: The Status Quo



Silvia Mittler

Abstract In the last few years Waveguide Evanescent Field Fluorescence (WEFF) and Scattering (WEFS) microscopy were developed which are alternatives to TIR and TIRF microscopy. Both technologies implement a slab waveguide-microscopy chip with a coupling grating. The technologies are described and compared to TIR and TIRF microscopy. The advantages of the waveguide method are clearly addressed. A brief history of the technology's development and similar activities in the field are discussed. Application examples from both WEF microscopies follow: static distance mapping with a multimode waveguide, dynamic solubilisation studies of cell plasma membranes and the kinetic response of osteoblasts to trypsin (WEFF); bacteria sterilization as well as cell adhesion and granularity studies (WEFS). The combination of both methods is discussed and found not suitable. In order to mass fabricate the necessary waveguide chips with the grating an all-polymer-waveguide chip was developed. This should allow to bring the new microscopy methods to the interested scientific community.

1.1 Introduction

With the aim of developing new medical devices with direct tissue contact, drug delivery vehicles, and tissue engineering scaffolds, there has been increasing interest in recent years in the interactions of cells with both synthetic and natural biomaterials [1, 2]. In particular, the study of the contact regions between a cell and its substratum is of considerable interest as its investigation delivers *inter alia* information about the cytocompatibility of the substratum—the affinity of cells towards that particular surface. Promotion or inhibition of cell adhesion to synthetic and natural biomaterials is often crucial to the proper function of a particular device. Some information concerning these interactions, e.g. the lateral location and the density of

S. Mittler (✉)
Department of Physics and Astronomy, The University
of Western Ontario, London, ON, Canada
e-mail: smittler@uwo.ca

the adhesion sites, as well as their relationship to the actin stress fiber system, part of the cell's cytoskeleton, can be inferred from fluorescence microscopy of immunolabeled molecules involved in adhesion; typically, vinculin, a protein located within the multi-protein complex that anchors the adhesion to the cytoskeleton inside the cell [3]. These methods only deliver signals from the focus volume and no information about adhesion distances to the substratum. However, a direct and quantitative method to address the distance to the substratum is highly attractive. To address this need, different microscopic techniques based on electron microscopy [4] and optical means such as evanescent fields and interference techniques have been developed. Total internal reflection fluorescence (TIRF) [3, 5], surface plasmon resonance microscopy (SPRM) [6], interference fluorescence microscopy (IRM) [7], fluorescence interference contrast (FLIC) microscopy [8] and combinations thereof [3, 9] have been used to visualize and quantify these contacts. The contacts themselves had been discovered by interference reflection microscopy (IRM) in the 1970s [10].

Bacteria, on the other hand, are the most metabolically diverse group of organisms found in all natural environments including air, water and soil. Bacteria commonly occur with food sources and are also found within and on our bodies. However, concerns exist over contamination of food, water, and air by pathogenic bacteria [11] that can enter our bodies through ingestion, inhalation, cuts or lacerations [12]. Therefore, there is an increasing interest in bacterial contamination and the need for anti-bacterial surfaces not only for application in the food industry but also for medical and hygienic purposes [13]. Over two million hospital-acquired cases of infection are reported annually in the USA, which lead to approximately 100,000 deaths annually and added nearly \$5 billion to U.S. healthcare costs [14, 15]. Contamination of medical devices (e.g., catheters and implants) has been attributed to 45% of these infections [16]. Bacterial contamination of any surface typically begins with the initial adhesion of only a few cells that can then develop into a more structurally cohesive biofilm in less than 24 h when provided with suitable nutrient conditions sustaining metabolism and cell division [17]. Therefore, a better understanding of bacterial adhesion to surfaces is important for technical surface development and in biomedical applications. However, the precise measurement of bacterial adhesion to surfaces are difficult and time consuming because bacterial cells typically occur on the micrometer-scale and their adhesion forces are generally low, typically 0.1–100 nN [18]. Recent studies on the detection of bacteria on surfaces have focused on similar imaging systems as with cells such as optical [19] and fluorescent microscopy [20] to image the bacteria themselves or luminescence measurement of the presence of cells by ATP (adenosine triphosphate) detection systems [21]. Surface Plasmon Resonance (SPR) sensors [22], Nucleic Acid Detection [23], Optical Waveguide Lightmode Spectroscopy (short: waveguide spectroscopy) [24], Optical Leaky Waveguide Sensors [25], and Evanescent Mode Fiber Optic Sensors [26] have also been applied in order to detect biochemical toxins as signatures of bacteria.

In conclusion, it is important to have methods available which are able to investigate interfaces between a technical surface and a bacterium or cell.

In recent years, Total Internal Reflection Fluorescent (TIRF) microscopy has been demonstrated to be an effective method for studying cell-substrate interactions that

occur at surfaces and interfaces. Using TIRF microscopy, the behavior of various types of cells [27, 28] and bacteria [29, 30] near surfaces has been characterized. Total Internal Reflection (TIR) Microscopy utilizes the basic technology of TIRF without any fluorescence dyes present in the sample by creating an optical contrast due to scattering [31]. Recent studies have also demonstrated the use of TIR for imaging microbial adhesion.

This paper will give a brief history and literature overview as well as a review on biophysical applications of WEFF and WEFS microscopy on cells and bacteria and a short outlook on current developments on mass producible all-polymer-waveguide-chips to offer the methods to a broader user base.

1.2 Brief History

The waveguide evanescent field scattering (WEFS) technique was developed by Thoma et al. in 1997 [32, 33] for ultrathin technical structures on surfaces using conventional ion exchanged waveguides. Thoma et al. investigated the influence of the polarization direction of the mode and the mode number on the achieved scattering image contrast. It was found that with increasing mode number the contrast increased. TE modes depicted a better contrast than TM modes. Immersion of the samples in an aqueous solution decreased the contrast as the refractive index difference between scattering centers and the surrounding medium decreased.

Before the first cells were imaged evanescently with a waveguide, a series of approaches were made to combine established microscopy methods with a conventional waveguide and waveguide spectroscopy to on-line monitor e.g. adhesion and proliferation of cultured cells [34–36]. These attempts suffered from the small penetration depth of the evanescent fields into the cells of the used conventional waveguides. Therefore, Horvath et al. [37] proposed in 2005 reverse symmetry waveguides which provided deeper penetrating evanescent fields in these combination technologies.

The first waveguide evanescent field fluorescence (WEFF) experiment with commercial mono-mode glass waveguides (designed for sensing on coupling gratings) on cells was shown by Grandin et al. [38]. Vinculin staining was carried out on fixed human fibroblast cells. The coupling was carried out via a coupling grating located within the sample area. The image suffered from substantial artefacts and was very noisy in form of stripes. The grating position in the field of view, lead to too many scattered photons and to resonantly out-coupled light.

WEFF microscopy with ion exchanged mono- or multi-mode glass waveguides and stained cell's plasma membranes was developed by Hassanzadeh et al. [39] in 2008 as a straightforward alternative to TIRF microscopy for imaging ultrathin films and cell-substrate interaction. The mode coupling was achieved via a grating coupler outside the imaging area. The image quality was increasing, but artefacts due to scattered light were still seen in the images and are not completely avoidable. TIRF images share the same issues [40]. Hassanzadeh et al. have then shown applications of WEFF microscopy with static and dynamic investigations [39, 41, 42]. They were

the first who used a multi-mode waveguides with mode selective grating coupling to determine distances of cell adhesions to the waveguide surface [43].

A year later, 2009, Agnarsson et al. [44] presented a symmetric waveguide structure for WEFF microscopy where the cladding material is index-matched to the sample solution (aqueous media). The optical chips were fabricated from polymers involving standard cleanroom technologies such as spin-coating, photolithography and dry etching (core: polymethylmethacrylate (PMMA) and substrate: amorphous perfluorinated optical polymer (Cytop)). Agnarsson et al. coupled via end-fire coupling mode-insensitive into a mono-mode waveguide. MCF7 breast cancer cells immune-stained with monoclonal antibody against the transmembrane adhesion protein E-cadherin (HECD-1) and Alexa Fluor 546 Goat Anti Mouse IgG1 fluorescent secondary antibody. Very clear WEFF images were obtained with some minor scattering artefacts. Agnarsson et al. were combining WEFF microscopy on the mono-mode polymer symmetric waveguide structures with waveguide spectroscopy and channel waveguide operation (directional couplers, ring resonators, Mach-Zehnder interferometers, etc.) for sensing application and on-chip control of illumination with sub-millisecond control [45–48].

In 2014, Nahar et al. [49] implemented WEFS microscopy for bacteria studies and started to investigate cultured osteoblasts with WEFS microscopy.

Agnarsson et al. [50] picked up WEFS microscopy in 2015 for label-free sensing of gold nanoparticles (AuNPs), vesicles and living cells, and compared it with WEFF results, all on symmetric polymer waveguide structures.

The focus of the following sections will be the WEFF and WEFS studies of the author's group.

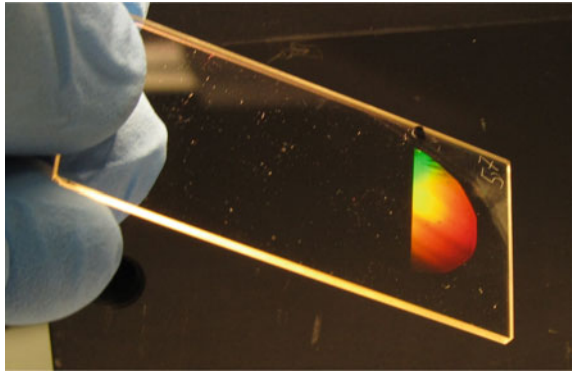
1.3 Experimental

1.3.1 Waveguides

Home-made, glass waveguides on fused silica (step-index slab waveguides) or ion exchanged waveguides with holographic coupling gratings will be addressed here [41, 51]. The waveguides were reusable various times after thorough cleaning. Cleaning procedure consisted sonification in 70% ethanol for 20 min followed by blow-dry with nitrogen gas. To remove organic material, the dried samples were cleaned with Nano-Strip (KMG Chemicals Inc., Fremont, CA, USA) at 80 °C for 5 min. After Nano-Strip application, the substrates were extensively rinsed in Milli-Q water and blown dry again [52]. However, with each cleaning cycle the waveguides became thinner and needed characterization before every new experiment.

The samples were designed in a way that the coupling grating is always kept outside the sample area and should not be altered during the experiment to keep the coupling conditions and therefore, the coupling efficiency, constant, Fig. 1.1. This is important because the mode coupling conditions change when material is adsorbed

Fig. 1.1 General WEFF- and WEFS chip design: the coupling grating is located outside the sample area



or desorbed at the grating position [53]. In addition, out-coupled photons from the grating produces artefacts in the WEFF and WEFS images. Any periodic structures should be avoided in the sample area due to undesired interference effects.

1.3.2 Cell Culture

The cell culture was according with [52] will be transcribed here. Osteoblastic cell line MC3T3-E1 (subclone 4, ATTC Catalog 3 CRL-2593) culture was carried out in flasks. Three hours UV light exposure was used to sterilize cleaned waveguides. Growth medium was prepared from 17.8 ml α -minimum essential medium 1X (MEM; Gibco), 2 mL fetal bovine serum (FBS; Gibco) and 0.2 mL antibiotic-antimycotic solution 100X (Anti-Anti; Gibco). First the medium was aspirated from the cell culture flask. Dulbecco's phosphate-buffered saline 1X (PBS; Gibco) was added to wash the cell layer and aspirated subsequently. To detach the osteoblasts from the vessel, wall, 5 ml trypsin-EDTA (0.05%, Gibco) was added and incubated at 37 °C for 5 min. The cell culture was checked by phase-contrast microscopy in order to confirm cells release into the suspension. Trypsin neutralization was carried out by adding 9 mL growth medium. The resulting cell suspension was then diluted in growth medium to 10,000 cells per mL. The waveguides were placed in a Petri dish and 1 mL cell suspension was deposited per surface. Samples were then incubated for 24 h at 37 °C, 100% humidity and 5% CO₂.

After incubation the waveguides were removed from the growth medium and excess medium was drawn. Each waveguide was then rinsed three times in PBS. For fixing waveguides with cells on top, were placed in a 4% paraformaldehyde solution in PBS for 10 min at room temperature. Subsequently, samples were rinsed three times with PBS. Desiccation was prevented, by keeping the samples in PBS until further treatment. A 1.5 mg DiO in 1 mL dimethyl sulfoxide (DMSO) solution was prepared and heated to 37 °C for 5 min. This solution was then sedimented for 5 min at 2000 rpm in order to separate solid residues. The staining solution was achieved

by taking of 10 μL of this solution and dissolving it in 1 mL of growth medium. A volume of 200 μL this solution was then pipetted onto the corner of each waveguide, which were gently agitated until complete cell coverage by the solution. These samples were left for 20 min in the solution to guarantee the incorporation of the dye. Afterwards, the staining solution was drained and PBS was used to wash the waveguides. For the removal of all unbound dye, the samples were immersed in PBS for 10 min and drained again. The wash cycle was repeated two more times. The waveguides were stored in PBS until performing WEFF microscopy. This procedure delivers fixed cells, cells that are “frozen” in their habitus [52, 54–56] with the dye situated in the plasma membrane of the cells.

1.3.3 Bacterial Culture

The bacterial culture has been previously described [52] will be transcribed here for consistency.

Nitrobacter sp. 263 was cultured on R2A (Difco™) plates at room temperature (approximately 23 °C) for two weeks. For each colonization experiment, bacteria from one R2A plate were removed and suspended in 1 ml of filter-sterilized (0.45 μm pore-size) distilled deionized water to produce an aqueous bacterial suspension (with 10^6 bacteria/ml). A distinct R2B stock solution (i.e., broth/liquid culture medium) was prepared by dissolving R2A in sterile, distilled, deionized water and filtering to remove the agar constituent keeping the dissolved nutrients for bacterial growth.

Attachment of the bacteria to the waveguide surface was attained by placing a 50 μl aliquot of the bacterial suspension on waveguide top for 1 h at 37 °C. After bacteria attachment, the waveguide was rinsed with sterile, distilled water and placed in a sterile Petri dish with 20 ml of R2A and after incubated for 24 h at 37° to allow bacteria to grow. These samples were not agitated. After 24 h incubation, bright field microscopy was used to examine the waveguides in looking for microcolonies formation. Images were taken of live cells in growth medium. WEFS microscopy was then used to analyse the samples. Sterilization experiments were undertaken. For this separate bacteria suspensions of 10 ml (with 10^6 bacteria/ml) were placed in a sterile, open glass dish and exposed, in a low pressure collimate beam apparatus (LPCB) [52, 57, 58] to doses of 2, 4, 8, 14, 20 and 30 mJ/cm^2 [52, 58]. This sterilization by UV photon was chosen mainly for its ability to disrupt and dimerize neighboring DNA bases (thymine dimerization) that hinders bacterial growth but not viability [52, 59, 60]. The ‘sterilized’ bacterial suspensions, obtained for the different dose exposures, were used in colonization experiments identical to those described above.

Before the first and second colonization assays, separate 1 mL aliquots of all bacterial suspensions were stained using BacLight™ (Invitrogen) Live-Dead stain and examined using fluorescence microscopy in order to confirm that the cells were viable.

1.3.4 Microscopic Analysis: WEFF and WEFS

An inverted microscope from Zeiss, Oberkochen, Germany, with the waveguide located on the sample stage was used for the WEFF and WEFS microscope assemblies consisted of an inverted microscope (Figs. 1.2 and 1.3). The specimen was placed on the waveguide's top. An argon ion laser (35 LAP 341-200, CVI Melles Griot) working at $\lambda = 488$ nm with a tuneable output power in the 7–126 mW range or a 0.5 mW, 543.8 nm HeNe laser from Research Electro-Optics, were used as light sources in WEFF and WEFS assemblies, respectively. The laser power was reduced by placing a neutral density filter directly behind the laser, avoiding overexposure and bleaching. The beam diameter was controlled by means of an iris aperture. A coupling grating located on the waveguide was used to couple the laser beam in the waveguide to a chosen mode. For the case of WEFF microscopy, undesired excitation wavelength was blocked via a long pass filter with a 490 nm cut-off wavelength (3RD490LP, Omega Optics, Brattleboro, VT), placed between the objective and the camera. The out-coupled intensity at the waveguide end was measured by a large active area photodiode (FDS1010, Thorlabs, Newton, NY) for determining the coupling efficiency when required. A cooled CCD-camera (Pursuit—XS 1.4 Diagnostic Instruments Inc., Sterling Heights, MI, USA), controlled with SPOT 5 Basic (Spot Image Solutions, Sterling Heights, MI, USA) was used for imaging. Bright field microscopy images of the samples were also obtained with the same field of view objective-lens as in the WEFF/WEFS microscopy images and processed through Image Pro Express software facilities (Media Cybernetics, Rockville, MD).

The laser beam coupling can be from below the waveguide chip in parallel to the objective lens as depicted in Fig. 1.2. This has the advantage that all beam steering can be done on the optical table. The disadvantage is the close proximity to the objective lens which restricts the available coupling angle substantially and forbids backward coupling.

In the alternative design the coupling is carried out from the top (Fig. 1.3). The advantage here is a restriction less coupling angle. The disadvantages are the possible

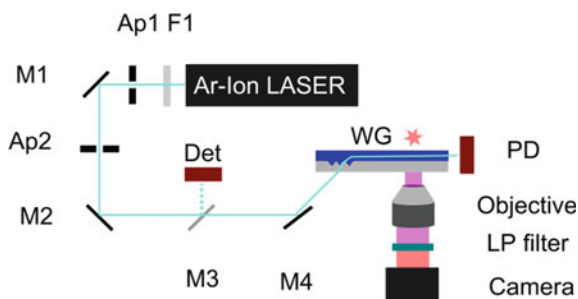


Fig. 1.2 Schematic of WEFF microscope with coupling through the waveguide chip from below: Ap—apertures, F1—neutral density filter, M—mirrors, WG—waveguide and PD—photo diode. For WEFS microscopy a HeNe laser was used and the LP filter omitted [52]

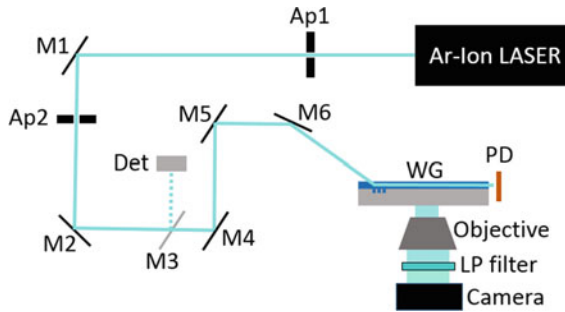


Fig. 1.3 Schematic of a WEFS microscope with coupling into the waveguide from above: Ap—apertures, M—mirrors, WG—waveguide and PD—photo diode. For WEFS microscopy a HeNe laser was used and the LP filter omitted. Optical elements Ap1 to M4 are mounted on the table

reflections and scattered photons from the objective lens, and some of the beam steering needs to be carried out above the optical table making the system more prone to vibration issues.

1.4 TIRF/TIR Versus WEFF/WEFS

Both TIRF/TIR and WEFF/WEFS microscopies assemblies, employ sample illumination through evanescent fields at the substrate surface which are coming from total internal reflection. In more recent TIRF/TIR microscopes a laser beam is optomechanically guided within the microscope and the objective lens, allowing a laser beam to undergo total internal reflection at a the high refractive index substrate carrying the specimen and is placed above the objective lens. Specially designed objective lenses having high magnification and numerical aperture objectives together with built-in optical path control are required for microscope construction. All angles above critical angle of TIR can be theoretically achieved in this way, allowing the possibility to achieve different penetrations depths by using different angles. This feature can even be used to measure distances from the substrate surface [61]. From the practical point of view, the microscopes are set to particular angles, for achieving both high quality TIRF/TIR imaging and high quality epi-fluorescence or bright field.

Besides, manual operation of a TIRF/TIR microscope can readily give rise to the evanescent mode loss and consequently to a full specimen exposure to the laser beam and sample damage.

Reviewing the literature in particular with respect to the use of TIRF microscopy for distance measurements it can be seen that, besides Burmeister's excellent work by the middle of the 1990s [62], during the development stage of TIRF microscopy, very little has been published on exploring different penetration depths.

In regard to TIR microscopy is performed identically but excluding the dye from the samples and the necessary filter sets. Scattered photons instead of fluorescence photons are collected. Bright field images are taken for comparison since epi-fluorescence is not realizable. It should be pointed out that few distance work involving TIR microscopy have been reported so far [29]. This is not surprising since the scattering intensities are difficult to analyze because all refractive index fluctuations present in the evanescent field contribute to the signal and these are not necessarily controllable, in particular with living cultures producing extracellular matrix in the case of cells or extracellular polymeric substance (EPS) when imaging live bacteria.

In WEFF/WEFS microscopies, the waveguide modes resonances dictate the available evanescent fields and penetration depths. Thus the number of options is limited by the number of modes propagating in the waveguide. In TIRF and TIR microscopies, the evanescent field penetration depth of the is limited to ~ 200 nm, whereas a waveguide can yield penetrations depths from below 100 nm to over a μm , by refractive index tuning and thickness architecture of both core and cladding layers [44]. Extended illumination area over macroscopic dimensions can also be achieved from planar waveguides which is only limited by the attenuation of the propagating waveguide mode.

In addition, as the beam in WEFF/WEFS cannot escape from the waveguide; the WEFF and WEFS microscopies carry the intrinsic safety mechanism of sample overexposure and damage.

Well characterized waveguides where the evanescent fields and penetration depths are well known can be used for quantitative measurements [43].

WEFF and WEFS microscopies do not seek for state-of-the-art microscopes or objective lenses assemblies. Their technologies can be based on a few simple accessories and attachments to standard inverted microscopes. It is therefore straightforward to image the specimen in any magnification and field of view available due to standard long distance objective lenses by just turning the objective lens revolver without the necessity of beam stirring. Due to the evanescent field formation being taken care of by the substrate and completely independent from the entire microscope, different field of views or magnifications still deal with the same illumination conditions allowing direct comparison of images or measurements after changing magnification and field of view.

By enhancing the image acquisition integration time, epi-fluorescence images can be obtained. This is due to waveguide slightly scattering, which provides 3D excitation or scattering photons to the specimen.

Comparing TIRF and WEFF images of the same samples identical image information can be observed [40]. Both are diffraction limited, in such a way that lateral resolution is dependent on the working laser wavelength and highest magnification lens and its numerical aperture (NA) supported by the microscope used. Resolution in the z-direction (normal to the substrate) is about 7 nm for both types of microscopes.

For WEFF and WEFS microscopies wide use it is necessary to have easy access to and supply of inexpensive waveguide substrates. Thus, it is necessary to implement a mass producible waveguide-chip.

1.5 Multimode Waveguide Use to Static Distance Mapping

A 651 ± 2 nm thick waveguide with refractive index of $n = 1.840 \pm 0.001$ was used for distances mapping of a dye, located in the plasma membrane of fixed osteoblasts. For simulating the evanescent fields the volume above the waveguide was assumed to be water with a refractive index of 1.33. Two images taken with the TM_1 and TM_2 mode were used to calculate the dye distance map [52, 63].

The WEFF image in Fig. 1.4 depicts four osteoblasts well spread and indicating the nuclei and some cell extensions. The dye distance map shows lower distance-colors (blue to yellow) in the cells areas from in the range of 0, to ~ 130 nm. In the unoccupied area, the unstained medium, where the raw data do not show fluorescence, only noise is present. This is depicted as distances in the order of the penetration depth of the evanescent field i.e. $\sim 160 \pm 40$ nm (red pixels with yellow). In addition, isolated spots in the no-sample area (outside the cells) are seen in very dark blue. These spots are correlated to un-physical distance values below zero caused by microscopic damages of the waveguide. These un-physical distances should always be omitted in image interpretation. All four osteoblasts can be found in the distance map and cell outlines are similar to the cells depicted in the “epi-fluorescence” image. It should be noted that filopodia and the thinly spread cell body are more clearly seen in the distance map. The distance map (Fig. 1.4) does not depict any information about the nuclei. Not the entire cell body reached down very close to the surface, as expected. At some of the cells’ outer lines and at some extreme tips of the spread cells, small regions of only a few pixels in diameter were found with distances of ~ 10 – 25 nm, typical of a focal adhesion [4, 64]. Twice line like accumulations of dense focal adhesions are found (blue lines with distances around 10–25 nm). Between the focal adhesions, there are regions in lighter blue depicting distances around 40–50 nm as well as greenish areas depicting distances around 70–80 nm. Filopodia of the cells, which are very faintly seen in the epi-fluorescence images, are clearly visible in the distance map as thin spikes with a blue (possible focal adhesions or point contacts) or green (possible extracellular matrix contacts) center and green-yellow surroundings [64].

Figure 1.5 depicts one well spread osteoblast taken in epi-fluorescence WEFF mode and false color distance map [49]. Two z-cuts through the distance map have been made: one randomly through the cell, (Fig. 1.5c) and one through an area including the smallest distances of the cell (Fig. 1.5d) [52]. The area outside the cell revealed to be nearly homogeneously dark red colored. The noise level in the no-sample regions is clearly seen in the z-cut data; it is the noisy data at an average distance of ~ 90 nm on both cell sides [52]. The cell itself is shown by the depressions in the z-cuts with the dips indicating adhesions. The spreading of the cell is excellently depicted by the distance map.

The cell is attached at all extreme spreading points, however not necessarily as focal adhesions since, distances above 40 nm and up to 50 nm, possible close contacts, are found. In the cell center, focal adhesions can be seen.

From the z-cuts the position of the plasma membrane/dye location along the cut line in nm can be seen. For the random ‘c’ cut, three “small” distances in the order

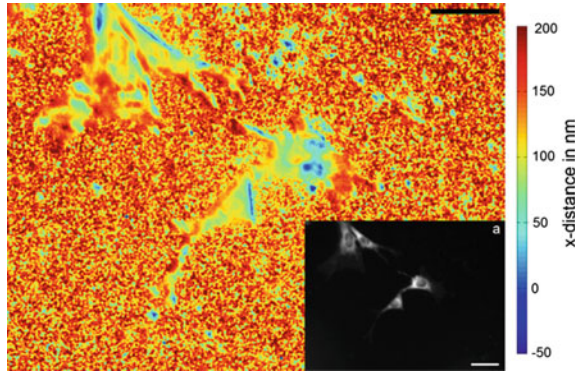


Fig. 1.4 Dye distance map with four osteoblasts, false color representation. The inset represents a WEFF image with increased integration time of the same field of view. Both scale bars represent 50 μm [52]

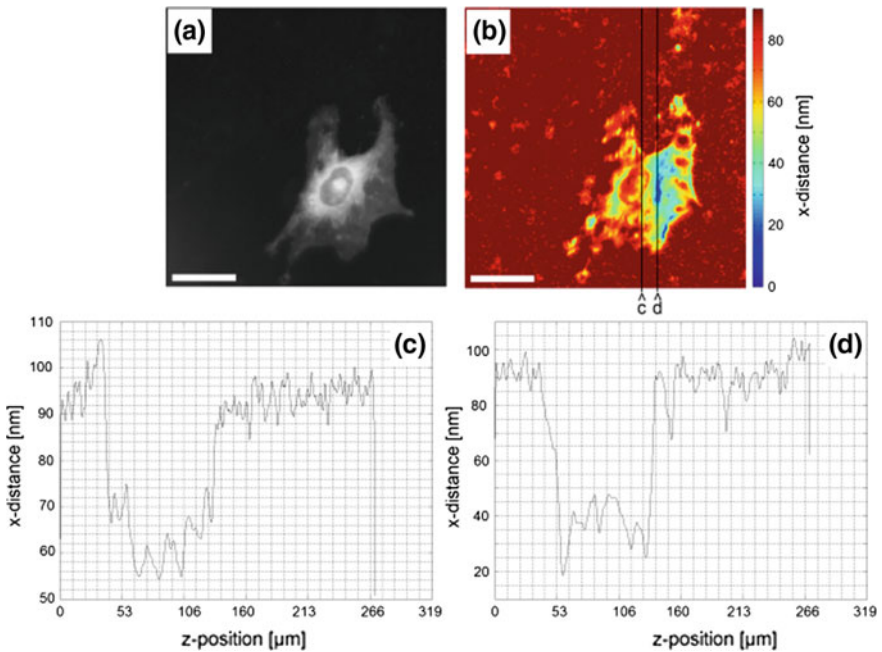


Fig. 1.5 Single osteoblast imaging results: **a** epi-fluorescence WEFF image, **b** dye distance map false color representation, **c** z-cut through cell at random position 'c' in part (b) and **d** z-cut through cell at smallest distance locations at position 'd' in (b). The cuts in (b) from bottom to top are represented in (c) and (d) from left to right. The scale bars represent 25 μm [52]

of ~ 55 nm are found, as well as a couple of more bends towards the substratum with distances of ~ 62 – 67 nm [52]. The maximum heights of the plasma membrane from

the waveguide surfaces between the bends towards the substratum are found to be between 62 and 75 nm.

In the z-cut ‘d’ through the small distance adhesions one 18 nm focal adhesion can be found as well as 25–35 nm distance contacts. The maximum heights of the plasma membrane from the waveguide surfaces in this case are 37 and 45 nm. The bending of the membrane towards the cytoplasm between these adhesions points is clearly depicted. The relative straight lines between the “maxima and minima” in the distance curve bear a resemblance to a stretched rubber band. One needs to keep in mind that the surface tension of the plasma membrane tries to minimize the surface area, trying to force the cell into a spherical shape. The adhesions are obvious biological disruptions of the physical effect of surface minimization.

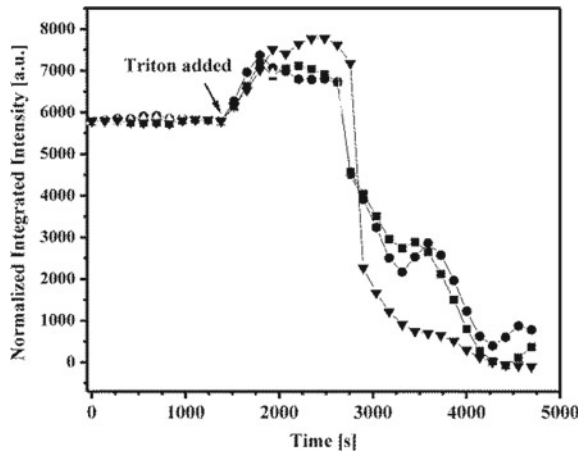
It would be interesting to monitor and quantitatively analyze the dynamics of a living cell moving and forming lamellipodia and new adhesions as well as retrieving lamellipodia and withdraw adhesion. With the current set-up, time laps distance mapping it is not yet possible. An automated, motorized mirror adjustment for M4 (Fig. 1.2) with a feedback loop for optimized coupling from the photodiode PD (Fig. 1.2) needs to be implemented.

1.6 Cell Plasma Membranes Dynamic Solubilisation Studies

Detergent-membrane interactions have been the subject of many studies [65]. Functional membranes typically exist in the fluid state, also called the liquid-disordered state. Due to difficulties of working with authentic cell membranes, simplified membrane models—such as supported lipid bilayers or liposome mimicking biological systems—have often been used to investigate detergent-membrane interactions [65]. Model membranes were helpful in exploring the basic membrane functions. However, in comparison to a living cell, with integral and peripheral proteins, cholesterol molecules and oligosaccharides in and on their plasma membrane, artificial membrane models cannot mimic all aspects of plasma membrane function. In addition, studying the interaction between lipids and detergents in the form of vesicles (liposomes) or supported lipid bilayers has several other disadvantages. For example, in supported lipid bilayers, the quality of the deposited film plays a major role. The direct contact with the underlying substrate affects the bilayer’s structure and fluidity, and blocks access of solutions to both sides of the membrane.

The results of lipid-detergent interaction studies using bio-membrane models have been related to a three-stage model, which was described by Lichtenberg et al. [66]. In stage I, with increasing detergent concentration, detergent incorporates into the bilayer. At this stage, solubilization does not occur, but the bilayer becomes saturated with detergent. At stage II, with further increase in detergent concentration, the bilayer starts to solubilise. Lipid vesicles saturated with detergent form and

Fig. 1.6 Three cells normalized integrated intensities versus time. Triton X-100 (0.013 w/w%) addition is indicated by the arrow [52]



coexist with mixed micelles of lipid and detergent. At stage III, the entire membrane solubilises, and only mixed micelles exist [67, 68].

Osteoblast were cultured on the waveguides and imaged alive with time laps WEFF microscopy. At a certain time Triton X-100 was added to the medium to start solubilisation. Figure 1.6 shows the normalized integrated intensity of the WEFF fluorescence signal of three example cells imaged with time.

Without detergent, the integrated intensities are constant indicating negligible photo bleaching. In the presence of detergent, three reproducible kinetic stages can be seen: (i) an increase in fluorescence intensity, (ii) a plateau, and (iii) a decrease in intensity. Therefore, a comparison to or an adaption of the established three-stage model is possible. In stage I, the membrane takes up detergent and the concentration of detergent rises in the plasma membrane. The integrated fluorescence intensity increases due to suppression of fluorophore quenching by dilution of the dye with detergent [69] in the cell membrane. In this stage, solubilisation does not occur. According to the model, stage I ends when the membrane becomes saturated with detergent [42]. The end of stage I is seen in Fig. 1.6 when the intensity increase ends and the plateau starts.

In stage II, where artificial membrane solubilisation takes place, the detergent-saturated lipid bilayer undergoes a structural transition and converts partially into lipid-detergent mixed micelles; however, these micelles are not yet mobile, but still incorporated in the membrane. So, stage II can be seen as the plateau in which intensity remains constant as the dye is not leaving the evanescent field. At this time, the dye is still located either in the membrane or in formed micelles in unquenched conditions mixed with detergent.

During stage III, the micelles become mobile and leave the evanescent field, leading to a decrease in integrated intensity. Individual micelles are too small to be seen with the WEFF microscope.

By changing the Triton X-100 concentration the duration of all three phases changed: the higher the detergent concentration the quicker the solubilisation stages [42].

WEFF microscopy confirmed that living osteoblasts are solubilized in the same way as model membranes.

1.7 Time Response of Osteoblasts to Trypsin

Trypsin is a serine protease and cleaves peptide chains. Therefore, trypsin is used in laboratories to cleave proteins bonding the cultured cells to the dish, so that the cells can be suspended in fresh solution and transferred to fresh dishes.

Healthy osteoblast cells were grown directly on the waveguide and monitored with time laps WEFF microscopy. Trypsin was used at 0.05 and 0.02% concentration. Upon addition of 0.05% trypsin, the cells were lifted very fast and only individual focal adhesions could be imaged. However, with the lower concentration changes in cell morphology could be observed, such as cell retraction.

The quick disappearance of an individual adhesion point at the high trypsin concentration was examined. The focal adhesion point had the appearance of a bright circular dot. A series of images were taken with time and analyzed. Figure 1.7 depicts the kinetic behaviour of the adhesion point's disappearance, with respect of its integral intensity and size. Clearly both the size and the integral intensity of this individual focal adhesion point decreased in an S-shaped curve and provided basically identical kinetic information about the detachment of the cell.

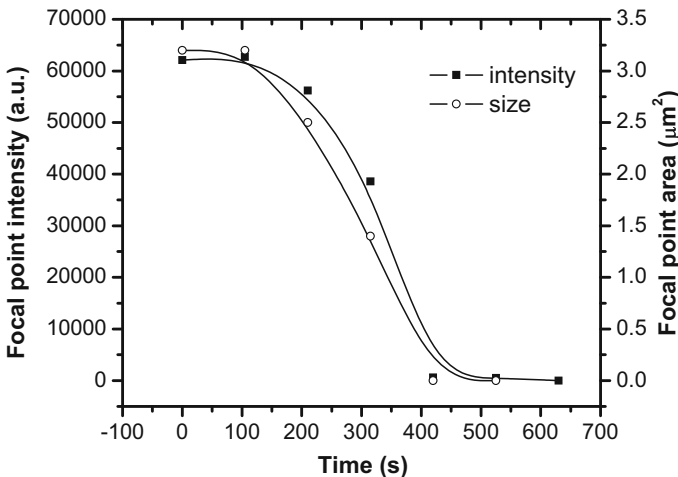


Fig. 1.7 The impact of a 0.05% trypsin containing medium on an individual focal adhesion: intensity and size decrease with time. The lines are guides to the eye [52]

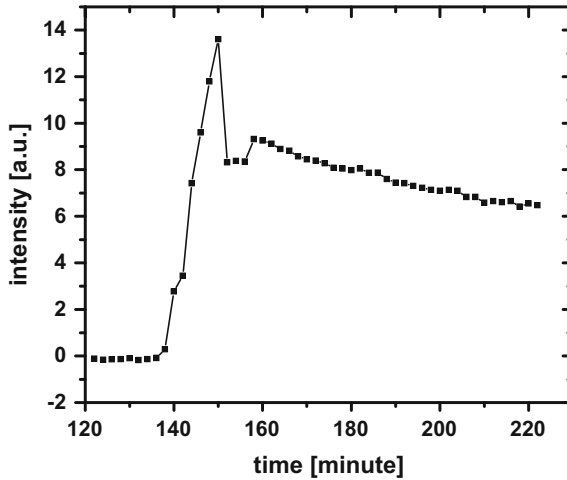


Fig. 1.8 Integrated, intensity of 5 individual re-appearing adhesion points after exchanging a trypsin-containing medium at $t=0$ to a trypsin-free medium [52]

A sample was treated with 0.02% trypsin. The cells have shown cell retraction, and detached from the surface, leaving a black feature less evanescent image. After the trypsin treatment the medium was exchanged carefully to a trypsin-free environment. The imaging was continued. The osteoblasts, still alive, re-synthesise new adhesion proteins for the formation of new adhesion points. The kinetics of the adhesion process, until the cell population died at around 150 min and lost adhesion again, is depicted in Fig. 1.8.

1.8 Bacteria Sterilization

Studies on the attachment of bacteria onto surfaces using WEFS microscopy detection is a quick method for investigations regarding bacterial sterilization treatment [49]. We hypothesized that non-potent, sterilized cells do not attach to surfaces and do not form microcolonies. Therefore, we have treated identical bacteria sample batches with different UV doses (2, 4, 8, 14, 20 and 30 mJ/cm^2). After the UV illumination the viability was measured. The UV illumination did not result in bacterial death. As a control, one sample was left without UV treatment. All bacteria illuminated with different UV doses and the control were cultured identically and examined using WEFS microscopy after 24 h. Figure 1.9 shows a series of WEFS and bright field images of the control and UV treated bacteria.

The relative signal attributed to attached colonies and individual bacteria on the waveguide surface decreased as exposure to UV illumination was increased (Fig. 1.9). It is significant to note that the highest dose of 30 mJ/cm^2 was not sufficient to completely prevent bacterial attachment. Both WEFS and bright field microscopy

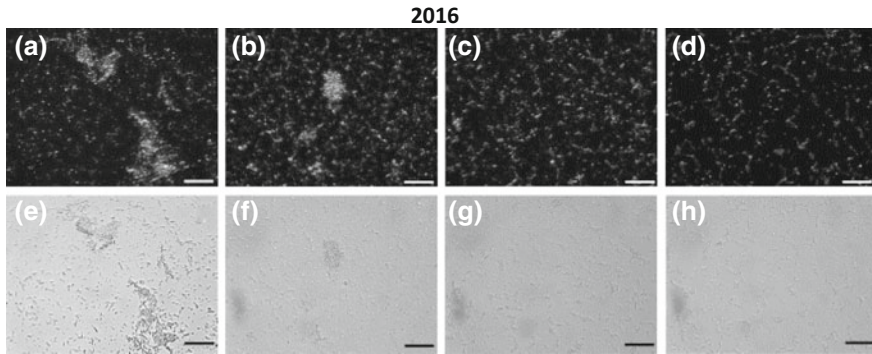


Fig. 1.9 WEFS and bright field microscopy images of UV illuminated, sterilized bacteria after 24 h of culturing: **a** and **e** control: 0 mJ/cm², **b** and **f** 8 mJ/cm², **c** and **g** 20 mJ/cm², **d** and **h** 30 mJ/cm². The scale bar is 50 μ m [52]

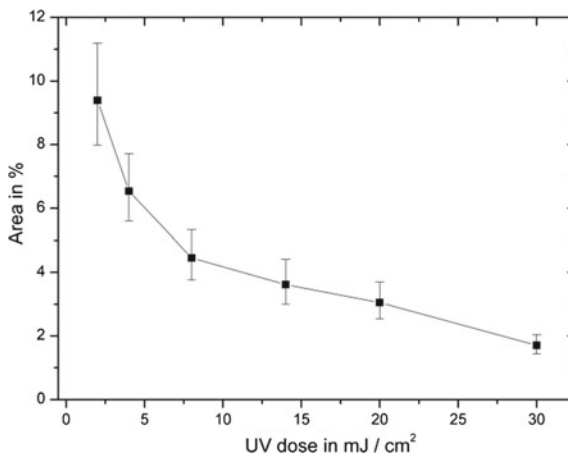


Fig. 1.10 Percentage of occupied area of bacteria versus applied UV dose. The line is a guide to the eye only

demonstrated that the highest dose resulted in the attachment of primarily individual bacteria, demonstrating that while attachment still occurred with increasing UV-dose, microcolony formation was prevented.

In order to yield quantitative data, a Matlab program was written to investigate the intensity distribution of each WEFS image and to calculate the percentage of area (i.e., pixels with signals above the defined threshold) occupied by bacteria (i.e., individual cells and cells comprising distinct colonies). Figure 1.10 shows the percentage of area on a sample occupied by bacteria versus the applied UV dose. Although the percentage of surface area with attached bacteria was decreasing exponentially, it did not reach zero. Bacteria were still attached to the waveguide surface despite the UV treatment. A “safe”-dose can be extrapolated by the data.

1.9 Cell Granularity and Adhesions

Fixed osteoblasts were imaged with WEFS microscopy. Figure 1.11 shows a bright field image of a single osteoblast and the corresponding WEFS image. In the WEFS image the nucleus can be located: it is the dark area in the cell center. In addition, the granular structures in the cell body and the adhesion sites at the cell outline were visible. Figure 1.11 indicates with the arrow the propagation direction of the waveguide mode. The cell's boundary first hit by the propagating light was shown very clear and with many adhesions points. The other three outer lines depict the adhesion points but not the complete cell boundary. At this chosen integration time the WEFS image depicts adhesions due to the evanescent illumination and the cell granularity due to 3D scattering of the waveguide.

Cell-substrate adhesions could be distinguished from scattering centers located further away from the substrate, the granularity of the cell, by varying the integration time. This is shown in Fig. 1.12.

With a very short integration time only a few spots appeared on the image in the areas where the cell was well spread. These spots are the cell's adhesions within the evanescent field. With increasing integration time, more and more features appeared, such as the cell nucleus area, the cells boundary and the cell granularity.

These experiments showed that not necessarily fluorescence staining was needed for imaging focal adhesions and hence getting some cell-substratum interaction measures. As in WEFF microscopy larger integration times lead to 3D information of the cell. Further detailed analysis, e.g. whether WEFS data are comparable with flow cytometry (scattering mode), need to be done.

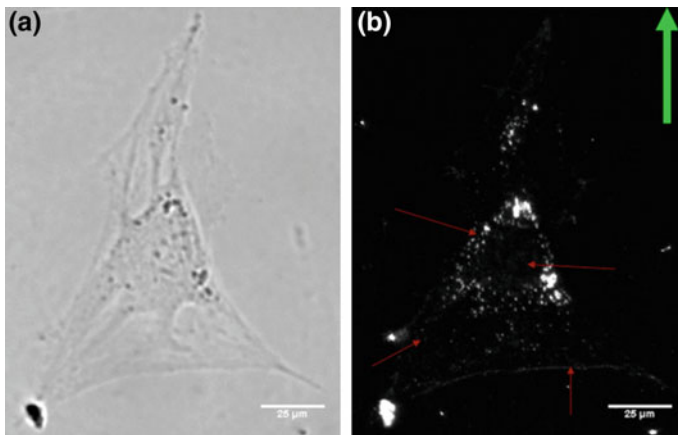


Fig. 1.11 **a** Bright field image and **b** WEFS image of an osteoblast taken with an exposure time 3000 ms. The green arrow indicates the direction of light propagation. The scale bars are 25 μm [52]

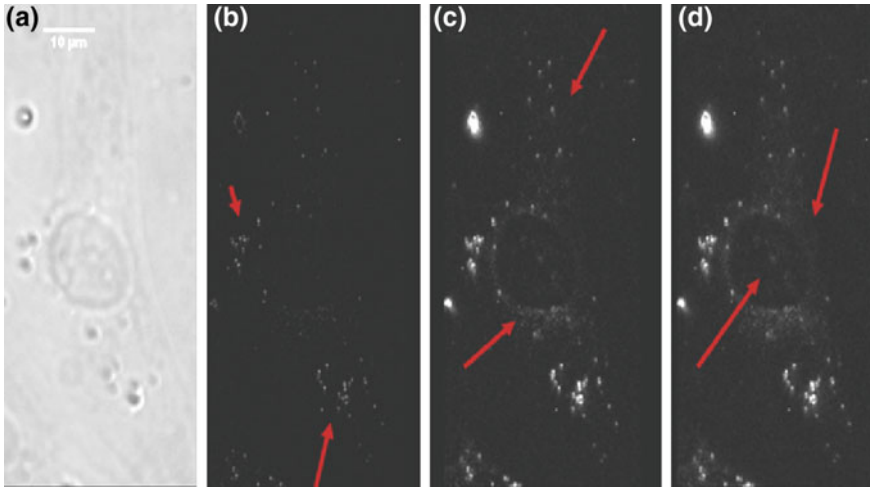


Fig. 1.12 **a** Bright field image of a single osteoblast and **b–d** corresponding WEFS images with integration times of 500 ms, 1000 ms and 1500 ms, respectively. The arrows point to the features mentioned in the text: **(b)** adhesions, **(c)** granularity and cell boundary, and **(d)** nucleus and cell boundary [52]

1.10 Imaging with WEFF/WEFS Microscopy

For evanescent imaging with WEFF and WEFS microscopy on the same sample, osteoblast cells were fixed and stained. The aim was to determine the information differences in the images taken with the various evanescent microscopy forms at identical samples and integration times. It is possible to image a stained object with WEFF microscopy implementing the long pass filter to block excitation light, with WFFS/WEFS combination microscopy by collecting both scattered excitation light and fluorescence photons, and with WEFS microscopy applying a short pass filter blocking the fluorescent emission wavelengths. Figure 1.13 shows a series of images of a single osteoblast taken with bright field, WEFF, WEFF/WEFS and WEFS microscopy.

Figure 1.13a shows the bright field microscopy image of a single osteoblast cell. The nucleus, and the outline of the cell were clearly visible in this image. To confirm the visualization of the entire cell with both WEFF and WEFS methods, an integration time of 6000 ms was used. The WEFF microscopy image is shown in Fig. 1.13b. Both the cell outline and cell body was distinctly visible in the WEFF image. The nucleus appeared black with some structure in it. The cell body was distinguishable from the other parts of the cell because of the presence of many densely packed bright spots around the nucleus. The outline of the cell which is actually the spread region of the cell was less bright than the rest of the cell but still unmistakable as it was identical to the bright field image of Fig. 1.13a. The white arrow in this image refers to the regions where the cell is touching an adjacent cell. The waveguide implemented here

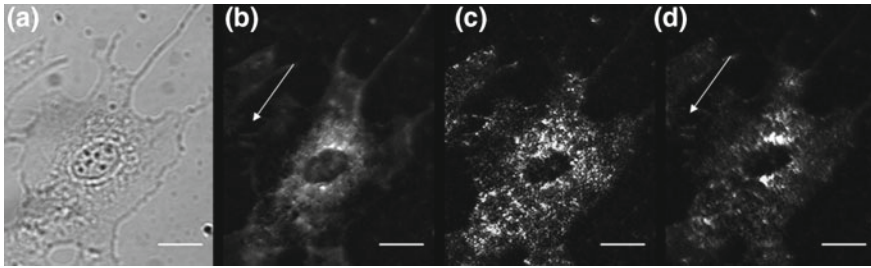


Fig. 1.13 Osteoblast imaged with a TM mode and 6000 ms integration time: **a** bright field image, **b** image captured with WEFF microscopy with a 560 nm long pass filter blocking excitation light of 543 nm, **c** WEFF/WEFS image captured without filters; hence both scattered and emission photons of the dye form the image, and **d** image captured with WEFS microscopy with a 550 nm short pass filter blocking the fluorescence. The arrows indicate where the cell is touching an adjacent cell. Scale bars represent 20 μm

has an evanescent field of 100 nm. Only the close contact regions of the cell should be visible in a “real” WEFF image. But due to the high integration time, the entire cell became visible as an epi-fluorescence image where parts of the cells located far away from the surface could also be seen. Close contact regions and focal adhesions are not possible to visualize with this types of WEFF imaging strategy.

Figure 1.13c shows the cell captured with no filters in WEFFS/WEFS combination mode. As a result, the scattered photons and the photons from the dye emission are forming the image. Although the cell outline was visible and nucleus distinguishable, there was too much intensity present in the entire cell making it impossible to distinguish the spread region of the cell and the cell body. Also the granularity was not visible as expected (Fig. 1.11).

Figure 1.13d, was captured with pure WEFS microscopy employing a 550 nm short pass filter blocking the fluorescence. This image showed the outline of the cells and the nucleus, but no clear distinguishing between the spread region of the cell and the cell body was possible. The links to the touching neighbor cell indicated by an arrow, were less prominent compared to the epi-fluorescence WEFF microscopy image. The granularity was distinctively different from the images of the cells which were not stained (Fig. 1.11).

From these studies it became clear that both methods have their individual optimum microscopy settings for achieving informative images. The amount of scattered light increased when a cell is stained and does not necessary deliver the same information about granularity as an unstained cell. Unresolved dye might act as additional scattering centers delivering artefacts. For an informative comparison of WEFF and WEFS images two sample sets should be prepared and imaged with individual optimized conditions (microscope settings and sample preparation).

1.11 All-Polymer-Waveguide-Chips

In order to allow WEFF and WEFS microscopy to be used by the interested communities, typically biophysics, biology, biochemistry and medical laboratories, but also for coating engineering (aging studies, homogeneity studies, anti-microbial tests, etc.) the waveguide chips need to be (commercially) available and at a reasonable cost. Mass production is the only way to accomplish this. An all-polymer-waveguide-chip with an imprinted coupling grating is one way to achieve this goal.

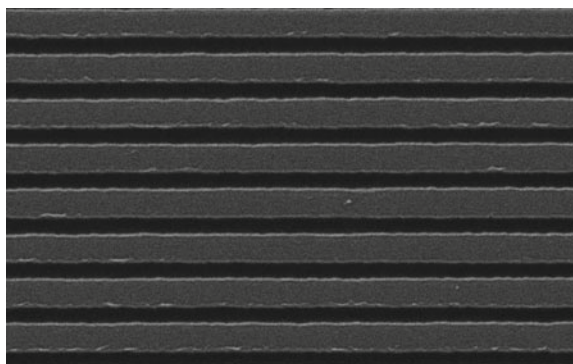
The all-polymer-waveguide chip was designed on the basis of a PMMA substrate.

The imprinting was performed into the PMMA with a home-fabricated silicon stamp, and in a subsequent step a polystyrene waveguide was spin coated on top.

Figure 1.14 shows an SEM image of an imprinted grating with a periodicity of 670 nm and a depth of 200 nm.

First experiments with the all-polymer-waveguide-chips have produced promising WEFF imaging results (Fig. 1.15). The WEFF image of the HeLa cell on the all-polymer-waveguide-chip does still look like an epi-fluorescence image. Also the distinct spotty or dotted pattern due to the adhesions at the end of the filopodia and at the outer rim of the cell are still missing. The polymer chips still suffer from too many scattered photons due to too many imperfections in the waveguide. The waveguide spin coating conditions need to be improved (dust free and with a homogeneous thickness throughout the sample). In addition, development towards mass produced chips is necessary. The grating of Fig. 1.11 and the all-polymer-waveguide-chip of Fig. 1.14 were fabricated by imprinting one grating into one PMMA substrate. The imprinting and waveguide spinning procedure needs to be scaled up to fabricate 16, 25, 36 or more chips in parallel on one substrate with one imprinting procedure and a subsequent high quality spin coating process and subsequent separation of the individual chips.

Fig. 1.14 SEM image of a PMMA imprinted coupling grating. The periodicity is 670 nm [52]



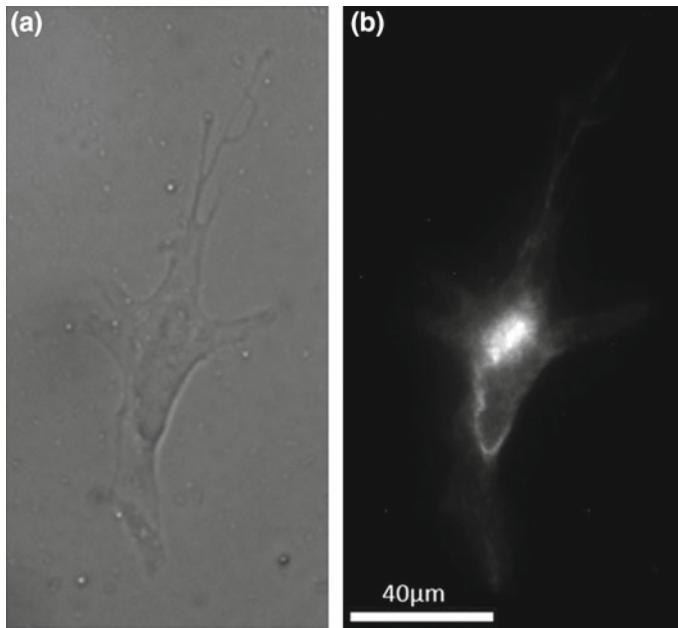


Fig. 1.15 All-polymer-waveguide-chip: **a** Bright field image and **b** WEFF image of a HeLa cell stained with DiO [52]

1.12 Conclusions and Outlook

A simple method to perform TIR and TIRF microscopy with a conventional inverted optical microscope by implementing an optical slab waveguide as the illumination source was discussed as well as the suite of advantages a confined beam in a waveguide offers in comparison to a standard TIR(F) microscope.

Both WEFF and WEFS microscopies were applied to a variety of biophysical questions: simple imaging of adhesions, quantitative investigations such as dye distance mapping and analyzing kinetic phenomena. A critical analysis of images taken in a WEFF/WEFS combination found that the combination is not recommendable. Each method should be used on samples especially prepared and with the optimum individual microscopy and image acquisition conditions.

In order to make the technology available for an interested scientific community, the availability of the waveguide-chip is essential. Therefore, a methodology for the fabrication of a mass produced, cost-effective waveguide-chip based on polymers only was developed and tested. In the future, the all-glass-chips should come with a surface functionalization allowing reusability. Time laps distance mapping is not possible yet, but planned.

Various types of interface and surface related biophysical and biological questions can be addressed with WEFF/S microscopy. They carry in addition the opportunity of

an implementation in sensor technology. Various options have been published already [45, 50].

There is a huge opportunity to also use WEF/FS for advanced measurements. The WEF/FS microscope can be simultaneously operated by propagating modes at different wavelength or directions for any kind of pump probe or resonance experiment, or a sensing scheme based on a Förster transfer in a dye upon binding of an analyte. Pulsed laser operation is another option. The scattering microscopy is responsive to any changes in the size or the refractive index (density) of the scattering entity within the evanescent field. The monitoring sensitivity of surface recognition reactions could easily be enhanced by increasing the scattering power by a gold nanoparticle [70] or by increasing the size of a scattering entity due to the binding [50].

Silane chemistry will allow to tune the waveguide's surface functionalization, both for all-glass and all-polymer-chips. Hydroxyl groups can easily be produced by oxygen plasma or UV ozone treatment for further functionalization [71, 72].

Acknowledgements Many co-workers, students, PhDs and colleagues are thanked for their contribution in the past, the present and the future for developing and applying WEF/FS and WEF/FS microscopy: Frank Thoma, Uwe Langbein, John J. Armitage, Hugu Trembley, Michael Nietzsche, Abdollah Hassanzadeh, Elisabeth Pruski, Jeffrey S. Dixon, Stephen Sims, Rebecca Stuchburry, Sabiha Hacibekiroglu, Daniel Imruck, Christopher Halpap, Michael Morawitz, Qamrun Nahar, Darryl K. Knight, Susanne Armstrong, Jeremia Shuster, Frederik Fleisser, Mihaela Stefan, Kibret Mequanint, Beth Gillies, Rene Harrison, Gordon Southam, Cheryle Seguin, Hong Hong Chen, Donglin Bai, Douglas Hamilton and Rony Sharon.

References

1. X.F. Niu, Y.L. Wang, Y.L. Luo, J. Xin, Y.G. Li, *J. Mater. Sci. Technol.* **21**, 571–576 (2005)
2. H. Storrie, M.O. Guler, S.N. Abu-Amara, T. Volberg, M. Rao, B. Geiger, S.I. Stupp, *Biomaterials* **28**, 4608–4618 (2007)
3. J.S. Burmeister, L.A. Olivier, W.M. Reichert, G.A. Truskey, *Biomaterials* **19**, 307–325 (1998)
4. W.T. Chen, S.J. Singer, *J. Cell Biol.* **95**, 205–222 (1982)
5. J.S. Burmeister, G.A. Truskey, J.L. Yarbough, W.M. Reichert, *Biotechnol. Prog.* **10**, 26–31 (1994)
6. K.F. Giebel, C. Bechinger, S. Herminghaus, M. Riedel, P. Leiderer, U. Weiland, M. Bastmeyer, *Biophys. J.* **76**, 509–516 (1999)
7. H. Verschuere, *J. Cell Sci.* **75**, 279–301 (1984)
8. B. Braun, P. Fromherz, *Appl. Phys. A-Mater. Sci. Process.* **65**, 341–348 (1997)
9. E. Atilgan, B. Ovaryn, *Curr. Pharm. Biotechnol.* **10**, 508–514 (2009)
10. M. Abercrombie, J.E. Heaysman, S.M. Pegrum, *Exp. Cell Res.* **67**, 359–367 (1971)
11. K.E. Sapsford, L.C. Shiver-Lake, in *Principles of Bacterial Detection: Biosensors, Recognition Receptors and Microsystems*, ed. by M. Zourob, S. Elwary, A.P.F. Turner (Springer, New York, 2008), pp. 109–123
12. J. Pizarro-Cerda, P. Cossart, *Cell* **124**, 715–725 (2006)
13. J.D. Oliver, *J. Microbiol.* **43**, 93–100 (2005)
14. A.E. Madkour, G.N. Tew, *Polym. Int.* **57**, 6 (2008)
15. A.E. Madkour, J.M. Dabkowski, K. Nusslein, G.N. Tew, *Langmuir* **25**, 1060–1067 (2009)
16. W.E. Stamm, *Ann. Int. Med.* **89**, 764–769 (1978)
17. E.M. Hetrick, M.H. Schoenfish, *Chem. Soc. Rev.* **35**, 780–789 (2006)

18. G.E. Christianson, 2004, in *Molecular Adhesion and Its Applications, The Sticky Universe*, ed. by K. Kendal, pp. 275–303
19. K. Vasilev, J. Cook, H.J. Griesser, *Expert Rev. Med. Devices* **6**, 553–567 (2009)
20. L. Pires, K. Sachsenheimer, T. Kleintschek, A. Waldbaur, T. Schwartz, B.E. Rapp, *Biosens. Bioelectron.* **47**, 157–163 (2013)
21. N.P. Pera, A. Kouki, S. Haataja, H.M. Branderhorst, R.M.J. Liskamp, G.M. Visser, J. Finne, R.J. Pieters, *Org. Biomol. Chem.* **8**, 2425–2429 (2010)
22. A.D. Taylor, J. Ladd, J. Homolas, S. Jang, in *Principles of Bacterial Detection: Biosensors, Recognition Receptors and Microsystems*, XXXII, ed. by M. Zourob, S. Elwary, A. Turner (Springer, 2008), pp. 83–108
23. M. Schmidt, M.K. Hourfar, S.-B. Nicol, A. Wahl, J. Heck, C. Weis, T. Tonn, H.-P. Spengler, T. Montag, E. Seifried, W.K. Roth, *Transfusion* **46**, 1367–1373 (2006)
24. I.R. Cooper, S.T. Meikle, G. Standen, G.W. Hanlon, M. Santin, *J. Microbiol. Methods* **78**, 40–44 (2009)
25. M. Zourob, S. Mohr, B.J.T. Brown, P.F. Fielden, M.B. McDonnell, N.J. Goddard, *Biosens. Bioelectron.* **21**, 293–302 (2005)
26. A. Mazhorova, A. Markov, A. Ng, R. Chinnappan, O. Skorobogata, M. Zourob, M. Skorobogatyy, *Opt. Express* **20**, 5344–5355 (2012)
27. A. Bauereiss, O. Welzel, J. Jung, S. Grosse-Holz, N. Lelental, P. Lewczuk, E.M. Wenzel, J. Kornhuber, T.W. Groemer, *Traffic* **16**, 655–675 (2015)
28. X. Liu, E.S. Welf, J.M. Haugh, J. R. Soc. Interface **12**, 20141412 (1–11) (2015)
29. L.V. Smith, L.K. Tamm, R.M. Ford, *Langmuir* **18**, 5247–5255 (2002)
30. M.A.S. Vigeant, M. Wagner, L.K. Tamm, R.M. Ford, *Langmuir* **17**, 2235–2242 (2001)
31. G.D. Byrne, M.C. Pitter, J. Zhang, F.H. Falcone, S. Stolnik, M.G. Somekh, *J. Microsc.* **231**, 168–179 (2008)
32. F. Thoma, U. Langbein, S. Mittler-Neher, *Opt. Commun.* **134**, 16–20 (1997)
33. F. Thoma, J.J. Armitage, H. Trembley, B. Menges, U. Langbein, S. Mittler-Neher, *Proc. SPIE* **3414**, 242–249 (1998)
34. T.S. Hug, J.E. Prenosil, M. Morbidelli, *Biosens. Bioelectron.* **16**, 865–874 (2001)
35. T.S. Hug, J.E. Prenosil, P. Maier, M. Morbidelli, *Biotechnol. Bioeng.* **80**, 213–221 (2002)
36. T.S. Hug, J.E. Prenosil, P. Maier, M. Morbidelli, *Biotechnol. Prog.* **18**, 1408–1413 (2002)
37. R. Horvath, H.C. Pedersen, N. Skivesen, D. Selmeczi, N.B. Larsen, *Appl. Phys. Lett.* **86**, 071101 (2005)
38. H.M. Grandin, B. Städler, M. Textor, J. Vörös, *Biosensens. Bioelectron.* **21**, 1476–1482 (2006)
39. A. Hassanzadeh, M. Nitsche, S. Mittler, S. Armstrong, J. Dixon, U. Langbein, *Appl. Phys. Lett.* **92**, 233503 (2008)
40. A. Hassanzadeh, M. Nitsche, S. Armstrong, N. Nabavi, R. Harrison, S.J. Dixon, U. Langbein, S. Mittler, *Biomed. Opt.* **15** 036018-1–036018-7 (2010)
41. A. Hassanzadeh, S. Mittler, *Opt. Eng.* **50**, 071103 (2011)
42. A. Hassanzadeh, H. Kan Ma, S.J. Dixon, S. Mittler, *Biomed. Opt.* **17**(076025), 1–7 (2012)
43. A. Hassanzadeh, S. Armstrong, S.J. Dixon, S. Mittler, *Appl. Phys. Lett.* **94**, 033503 (2009)
44. B. Agnarsson, S. Ingthorsson, T. Gudjonsson, K. Leosson, *Opt. Express* **17**, 5075–5082 (2009)
45. B. Agnarsson, J. Halldorsson, N. Arnfinnsdottir, S. Ingthorsson, T. Gudjonsson, K. Leosson, *Microelectron. Eng.* **87**, 56–61 (2010)
46. H. Keshmiri, B. Agnarsson, K. Leósson, *SPIE*, vol. 8090, 80900 D1-6 (2011)
47. B. Agnarsson, A.B. Jonsdottir, N.B. Arnfinnsdottir, K. Leosson, *Opt. Express* **19**, 22929–22935 (2011)
48. K. Leosson, B. Agnarsson, *Micromachines* **3**, 114–125 (2012)
49. Q. Nahar, F. Fleissner, J. Shuster, M. Morawitz, C. Halfpap, M. Stefan, G. Southam, U. Langbein, S. Mittler, *J. Biophotonics* **7**, 542–551 (2014)
50. B. Agnarsson, A. Lundgren, A. Gunnarsson, M. Rabe, A. Kunze, M. Mapar, L. Simonsson, M. Bally, V.P. Zhdanov, F. Höök, *ACS Nano* **9**, 11849–11862 (2015)
51. C. Halfpap, M. Morawitz, A. Peter, N. Detrez, S. Mittler, U. Langbein, *DGaO Proceedings*, 0287-2012 (2012)

52. S. Mittler, *Proceedings of the 4th International Conference on Photonics, Optics and Laser Technology, PHOTOPTICS 2016* (SciTePress, 2016), pp. 201–212
53. D.C. Adler, T.H. Ko, J.G. Fujimoto, Speckle reduction in optical coherence (2004)
54. R. Horvath, J. Vörös, R. Graf, G. Fricsovszky, M. Textor, L.R. Lindvold, N.D. Spencer, E. Papp, *Appl. Phys. B* **72**, 441–447 (2001)
55. L.L. Lanier, N.L. Warner, *J. Immunol. Methods* **47**, 25–30 (1981)
56. J.W. Smit, C.J.L.M. Meijer, F. Decay, T.M. Feltkamp, *J. Immunol. Methods* **6**, 93–98 (1974)
57. J.-W. Su, W.-C. Hsu, J.-W. Tjiu, C.-P. Chiang, C.-W. Huang, K.-B. Sunga, *J. Biomed. Opt.* **19**, 075007 (2014)
58. R.P. Hedrick, B. Petri, T.S. McDowell, K. Mukkatira, L.J. Sealey, *Dis. Aquat. Org.* **74**, 113–118 (2007)
59. J. Kuo, M. Asce, C.-L. Chen, M. Nellor, *J. Environ. Eng.* **129**, 774–779 (2003)
60. M. Berney, F. Hammes, F. Bosshard, H.-U. Weilenmann, T. Egli, *Appl. Environ. Microbiol.* **73**, 3283–3290 (2007)
61. B. Durbbeej, L.A. Eriksson, *J. Photochem. Photobiol. A: Chem.* **152**, 95–101 (2002)
62. G.A. Truskey, J.S. Burmeister, E. Grapa, W.M. Reichert, *J. Cell Sci.* **103**, 491–499 (1992)
63. J.S. Burmeister, G.A. Truskey, W.M. Reichert, *J. Microsc.-Oxford* **173**, 39–51 (1994)
64. F. Fleissner, M. Morawitz, S.J. Dixon, U. Langbein, S. Mittler, *J. Biophotonics* 1–12 (2014)
65. N. Tawil, E. Wilson, S. Carbonetto, *J. Cell Biol.* **120**, 261–271 (1993)
66. V.N. Ngassam, M.C. Howland, A. Sapuri-Butti, N. Rosidi, A.N. Parikh, *Soft Matter* **8**, 3734–3738 (2012)
67. D. Lichtenberg, J. Robson, E.A. Dennis, *Biochem. Biophys. Acta* **821**, 470–478 (1985)
68. G. Csucs, J.J. Ramsden, *Biochem. Biophys. Acta* **1369**, 304–308 (1998)
69. A. Helenius, K. Simons, *Biochem. Biophys. Acta* **415**, 29–79 (1975)
70. J.R. Silvius, *Annu. Rev. Biophys. Biomol. Struct.* **21**, 323–348 (1992)
71. A. Klein, Diploma Thesis, RheinMain University, Rüsseleheim, Germany (2008)
72. S. Kandeepan, J.A. Paquette, J.B. Gilroy, S. Mittler, *Chem. Vap. Depos.* **21**(275), 280 (2015)